JOURNAL OF MAGNETIC RESONANCE IMAGING 32:1217–1227 (2010)

Original Research

Reconstruction of 3D Dynamic Contrast-Enhanced Magnetic Resonance Imaging Using Nonlocal Means

Ganesh Adluru, PhD,[1*] Tolga Tasdizen, PhD,[2] Matthias C. Schabel, PhD,[1]
and Edward V.R. DiBella, PhD[1]

Purpose: To develop and test a nonlocal means-based reconstruction algorithm for undersampled 3D dynamic contrast-enhanced (DCE) magnetic resonance imaging (MRI) of tumors.

Materials and Methods: We propose a reconstruction technique that is based on the recently proposed nonlocal means (NLM) filter which can relax trade-offs in spatial and temporal resolutions in dynamic imaging. Unlike the original application of NLM for image denoising, the MR reconstruction framework here can offer high-quality images from undersampled *k*-space data. The method is based on enforcing similarity constraints in terms of neighborhoods of pixels rather than individual pixels. The method was applied on undersampled 3D DCE imaging of breast and brain tumor datasets and the results were compared to sliding window reconstructions and to a compressed sensing method using total variation constraints on the images.

Results: Undersampling factors of up to five were obtained with the proposed approach while preserving the spatial and temporal characteristics. The NLM reconstruction method offered improved performance over the sliding window and the total variation constrained reconstruction techniques.

Conclusion: The reconstruction framework here can give high-quality images from undersampled DCE MRI data and has the potential to improve the quality of DCE tumor imaging.

Key Words: DCE MRI; undersampling; nonlocal means; reconstruction; compressed sensing
J. Magn. Reson. Imaging 2010;32:1217–1227.

DYNAMIC CONTRAST-ENHANCED (DCE) magnetic resonance imaging (MRI) of tumors offers a promising means to assess tumor vascularity and vessel permeability (1,2). It can also be a valuable means to track the treatment response of novel drug therapies (3–5). The uptake and washout temporal characteristics along with the shape and spatial boundaries of the tumors offer useful information about their malignancy (6,7). High spatial resolution is required in order to be able to delineate the boundaries of small enhancing lesions (8). It has been demonstrated that high temporal resolution can increase the diagnostic accuracy by obtaining semiquantitative/quantitative parameters for kinetics of tumor enhancement following the injection of contrast agent using pharmacokinetic models (9,10). However, conventional data acquisition and reconstruction schemes are limited in terms of achieving desirable spatial and temporal resolutions simultaneously.

A number of frameworks have been proposed to overcome the trade-off in spatial and temporal resolutions in dynamic MRI. A comprehensive overview of all the reconstruction techniques is beyond the scope of this article; however, we mention some of the methods that have been applied or that are directly applicable to DCE tumor imaging. Parallel imaging techniques like SENSE (11) and GRAPPA (12) acquire undersampled *k*-space data for each time frame and use the coil sensitivity information to resolve the artifacts and are commercially available on most clinical scanners. SENSE was recently applied on a large breast cancer population and was found to shorten scan times over conventional acquisitions (13). These techniques, however, do not take into account the temporal redundancy in dynamic imaging, limiting achievable accelerations. In addition, parallel imaging techniques result in a signal-to-noise ratio (SNR) penalty in the reconstructed images.

Data sharing methods have been proposed that use data acquired from adjacent time frames to fill in the missing data (14,15), taking advantage of temporal correlations. A view-sharing method that fills in missing radial *k*-space lines in the current frame from adjacent time frames was applied on breast DCE acquisitions to remove streaking artifacts and to obtain high spatial resolution images (15). However, these methods cause temporal blurring of rapidly changing signals, especially around the spatial edges of small enhancing structures (15,16). The UNFOLD method is

---

[1] UCAIR, Department of Radiology, University of Utah, Salt Lake City, Utah, USA.

[2] Electrical & Computer Engineering, University of Utah, Salt Lake City, Utah, USA.

*Address reprint requests to: G.A., UCAIR, 729 Arapeen Dr., Salt Lake City, UT 84108. E-mail: gadluru@gmail.com

Received May 15, 2010; Accepted August 12, 2010.
DOI 10.1002/jmri.22358

a popular approach to capture rapid physiological changes in dynamic imaging by achieving high undersampling factors in *k*-space without significant loss in image quality. The method is based on application of a temporal lowpass filter (17). The method uses interleaved undersampling of data over different time frames to move the ghosting artifacts toward the ends of the temporal frequency spectrum and then removes them using a lowpass filter. The method was used to accelerate functional MRI (fMRI), cardiac cine imaging, and cardiac perfusion imaging (17,18). k-t BLAST method extended the UNFOLD approach by spatiotemporal filtering the undersampled data (19). The approach is based on a Wiener filter in which training data are used to obtain an estimate of the power spectrum of the signal estimate and a spatiotemporal filter is built to remove Nyquist undersampling artifacts in x-f space.

Hybrid methods combining dynamic imaging techniques with parallel imaging methods have also been proposed. A radial view-sharing method inplane was combined with SENSE encoding in slice dimension for accelerating bilateral breast DCE acquisitions (20). TSENSE approach (21) combined the UNFOLD method with SENSE reconstruction and was applied to 3D spiral breast imaging (22). Postprocessing methods like Independent Component Analysis have also been applied to remove streak artifacts from radial undersampling in breast DCE imaging (23). The feasibility of using the HYPR approach (24) for high spatial and high temporal resolution breast imaging has been demonstrated (25).

Recently, an inverse problem based total variation (TV) filtering has been extended to remove undersampling artifacts when reconstructing both static and dynamic MRI data (26–28). In the original application, the filter was applied to denoise images by iteratively minimizing a cost function consisting of an image fidelity term and an L_1 norm penalty term on image gradients (29). The method produced high-quality edge-preserving denoising for a variety of images including MR images (30). Unlike the denoising case, in the MR reconstruction problem data are acquired in *k*-space and we can incorporate information about the sampling pattern; fidelity is preserved only at the sampled locations and the same TV filter is applied to resolve the undersampling artifacts. This approach fits in the framework of compressed sensing, which suggests that exact reconstruction of sparse objects from undersampled Fourier data (below the Nyquist limit) is possible by minimizing the L_1 norm of sparse estimate (31,32). The approach was applied to a number of imaging scenarios and led to improvements in quality over conventional approaches. However, one limitation with the TV constraint is that it does not fully exploit the redundancies in images, as the intensity gradients are local and this results in a staircase effect in the reconstructed images with loss of fine texture (33). Also, since most MR images do not satisfy the piecewise constant model for TV, small image features which may be important can be lost (26,27,34).

Nonlocal means (NLM) is an image denoising method recently proposed by Buades et al (35). The fundamental idea of NLM is to reduce noise by averaging similar pixels regardless of whether they are spatially close or not. Based on a more statistical framework, an iterative unsupervised information-theoretic adaptive filtering (UINTA) denoising method was proposed at the same time (36). The methods produced state-of-the-art denoising results on a wide variety of images including ones with fine structures and texture. In the context of MRI, NLM was applied to denoise brain MR images after correcting the magnitude images for bias (37,38). Improved noise removal was achieved when the approach was extended to use multimodal images jointly (39). NLM denoising was also recently applied to real-time cardiac MRI acquisitions to improve the SNR (40). Unlike its previous applications for denoising, here we extend the NLM method to reconstruct images from undersampled *k*-space data. Motivation for using such a nonlocal constraint for MR reconstruction arises from the success of the neighborhood or patch-based nonlocal means denoising method over previous methods based on local features (37,38). Nonlocal constraints can serve as a better model for artifact-free MR images than gradient-based constraints and enforce self-similarity in terms of patches rather than individual pixels. Here we broaden the NLM-based reconstruction method used for 2D static MRI (41) to 3D dynamic imaging of tumors and also take into account the multicoil nature of MRI to obtain higher reduction factors.

The article is organized as follows. In the next section we first give an overview of the original NLM filter for general denoising and then build an MR reconstruction framework based on the filter for 3D dynamic reconstruction. Results are then presented using DCE data acquired from patients with breast and brain tumors and compared to existing methods. A discussion of aspects of the reconstruction including possible extensions follows.

MATERIALS AND METHODS

Nonlocal Means

A wide spectrum of images have inherent redundancy and this can be exploited to remove noise. In the NLM method, each pixel in a given noisy image is modeled as a weighted average of pixels in a large neighborhood surrounding it. These weights are assigned based on the amount of *similarity* to the given pixel. *Similarity* here is defined in terms of a distance between spatial neighborhoods surrounding the pixels. The distance between neighborhoods is computed based on differences in pixel intensities, as described below. The mathematical formulation of NLM is given as:

$$\hat{\mathbf{m}}(p) = \frac{\sum\limits_{q\in\Omega(p)} \mathbf{w}(p,q)\mathbf{m}(q)}{\sum\limits_{q\in\Omega(p)} \mathbf{w}(p,q)} \qquad [1]$$

Where $\hat{\mathbf{m}}$ is the filtered version of the given image, $\mathbf{m}$. p is the pixel of interest and $\Omega(p)$ is a large neighborhood of pixels around p (search window), $\mathbf{w}(p,q)$ is the weight for pixel q in $\Omega(p)$ which is computed as:

$$\mathbf{w}(p,q) = e^{\frac{-\mathbf{d}(p,q)}{h^2}}; \mathbf{d}(p,q) = ||\mathbf{m}(\mathbf{N}_p) - \mathbf{m}(\mathbf{N}_q)||^2_{2,a} \qquad [2]$$

$\mathbf{N}_\mathrm{p}$ and $\mathbf{N}_\mathrm{q}$ are identical in size and shape, smaller neighborhoods around p and q, respectively (comparison windows). $\mathbf{d}(p,q)$ is a Gaussian weighted Euclidean distance between the pixel intensities around p and q, and the parameter a is the variance of a Gaussian that gives decaying weights to pixel differences away from p and q (35). The parameter h controls the decay of the weights.

Reconstruction of Undersampled Dynamic Data

When k-space data are undersampled, artifacts arise in the images. The degradation in image quality depends on the amount and the type of undersampling and is not the same as that caused by adding more noise to the images. In order to resolve these undersampling artifacts we use a model-based approach built on a realistic nonlocal model for images (35). We apply the model constraints on the spatial and temporal characteristics of dynamic MR images. The spatial neighborhood constraint, S_{nbd} for a given time frame is a penalty functional given by:

$$s_{nbd} = \sum_{p \in tfr} \sum_{q \in \Omega_S(p)} \mathbf{w}_s(p,q) \parallel \mathbf{m}_p - \mathbf{m}_q \parallel_2^2 \qquad [3]$$

In Eq. [3], $\mathbf{m}$ is the reconstructed image estimate for the dynamic data, $\mathbf{m}_p$ and $\mathbf{m}_q$ are individual pixels p and q in a given time frame tfr, $\mathbf{\Omega_S}$ represents the 2D spatial search window and $\mathbf{w_s}$ represents the spatial weighting. Unlike gradient-based penalty terms, this constraint enforces similarity in terms of neighborhoods rather than adjacent pairs of pixels. In order to also model the temporal correlations, another neighborhood-based penalty term is used. For a given pixel time curve, tcr, this is computed as

$$T_{nbd} = \sum_{p \in tcr} \sum_{r \in \Omega_{T(p)}} \mathbf{w_t}(p,r) \parallel \mathbf{m}_p - \mathbf{m}_r \parallel_2^2 \qquad [4]$$

Where $\mathbf{m}_p$ and $\mathbf{m}_r$ represent pixels at timepoints p and r, $\Omega_\mathbf{T}$ represents the 1D temporal window and $\mathbf{w_t}$ represents the temporal weight.

Along with these spatial and temporal image constraints (S_{nbd} and T_{nbd}), a data fidelity constraint is needed to form the image reconstruction approach. Incorporating the k-space sampling pattern information and applying the Fourier transform, the data fidelity constraint is given by $\parallel \mathbf{Am} - \mathbf{d} \parallel_2^2$. $\mathbf{A}$ denotes the forward modeling operator on the image $\mathbf{m}$ to match the acquired data $\mathbf{d}$ from a single coil. In order to exploit the multicoil nature of the data acquisition, we modify this data fidelity constraint as:

$$F = \parallel \mathbf{Em} - \mathbf{D} \parallel_2^2 \qquad [5]$$

where $\mathbf{E}$ represents an operator with both coil sensitivity and k-space sampling information for all the coils and $\mathbf{D}$ is the data acquired from all coils (26). This penalty term ensures that the final reconstructed image estimate matches data acquired simultaneously from multiple coils.

Putting the above model constraints together, dynamic joint multicoil reconstruction uses the sum of T_{nbd} over all time curves and S_{nbd} over all time frames:

$$\begin{gathered}\min{}_m \left(\sum_{\forall tcr} T_{nbd}, \sum_{\forall tfr} S_{nbd} \right) \\ s.t. \parallel \mathbf{Em} - \mathbf{D} \parallel_2^2 < \varepsilon\end{gathered} \qquad [6]$$

where ε is a small positive constant related to the noise level.

This approach represents a general framework that results in reconstructed MR images that have similarity in neighborhoods rather than only in adjacent pixel values.

Implementation of the constrained reconstruction is performed in an iterative projections onto convex sets (POCS) framework (42). In every main iteration, the reconstructed image estimate is projected onto the multicoil data fidelity term and then Eq. [1] is applied in time and space in order to minimize Eqs. [4] and [5]. A similar alternating minimization POCS scheme has been used for L_1 constrained reconstruction. Note that applying the NLM filter in Eq. [1] on the image in space and time is equivalent to minimizing Eqs. [3] and [4], respectively. This is mathematically shown previously (43), where NLM was applied for super-resolution reconstruction of naturally occurring images.

The NLM formulation is more general than the gradient-based constraints, which minimize the local difference between pixels, for example, $T_{gradient} = \sum_{p \in tcr} \parallel \mathbf{m}_p - \mathbf{m}_{p-1} \|_1$ represents a temporal L_1 norm gradient constraint (28). In contrast to TV, the difference between each pixel and a larger neighborhood of pixels is minimized with a certain weighting in NLM. Figure 1 illustrates the idea of modeling the spatial and temporal characteristics using the neighborhood constraints using a DCE breast dataset. One single time frame from the dynamic sequence along with a time curve for pixel p is shown for illustrative purposes. The above NLM framework results in reconstructed images where each pixel p is modeled as a weighted average of pixels not only in the spatial search window $\Omega_\mathbf{s}$ but also in the temporal search window $\Omega_\mathbf{T}$. The weights for pixels in the search window are such that higher weights are given to pixels with similar comparison windows, for example, $\mathbf{S_p}$ and $\mathbf{S_q}$ have similar spatial comparison windows and $\mathbf{T_p}$ and $\mathbf{T_r}$ are similar in the temporal search window. This pushes similar pixels to be more similar while allowing differing pixels to be penalized less for maintaining their difference.

The implementation for NLM reconstruction of DCE MRI is:

1. Choose an initial guess: $\mathbf{m^0}$
2. Project the current image estimate onto the data consistency term: $\mathbf{m}^m_{data} = \mathbf{m}^n + \mathbf{E}'(\mathbf{D} - \mathbf{Em}^n)$, $\mathbf{E}'$ is

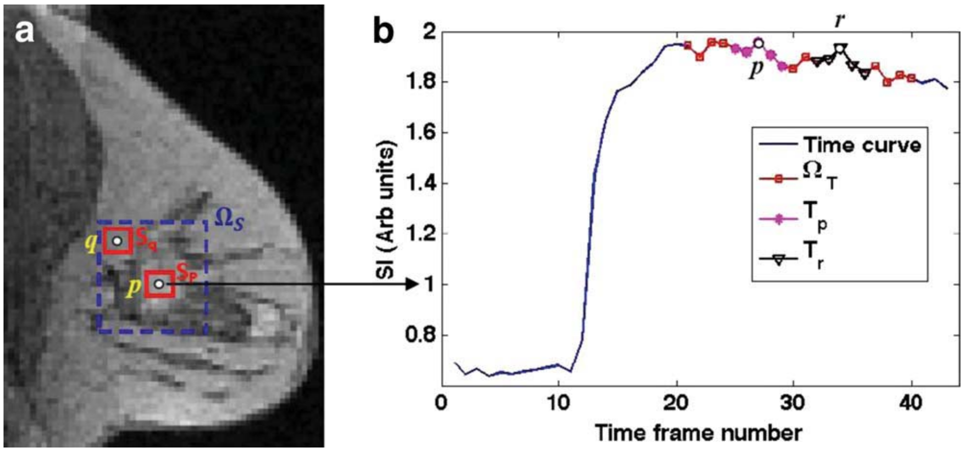

Figure 1. Illustration of modeling of DCE data with spatiotemporal neighborhoods. **(a)** Single time frame from a DCE breast sequence with a spatial search window $\Omega_\mathbf{S}$ around pixel *p*, and spatial comparison windows $\mathbf{S_p}$ and $\mathbf{S_q}$ around pixels *p* and *q*, respectively. **(b)** Illustrative time curve corresponding to pixel *p* along with 1D temporal search window $\Omega_\mathbf{T}$ around pixel *p* and temporal comparison windows $\mathbf{T_p}$ and $\mathbf{T_r}$ around timepoints *p* and *r*, respectively. Gaussian weighting is used for these spatial and temporal comparison windows to weigh more the central pixels.

the adjoint operator of **E**. Superscript *n* is the index for main iterations starting with 0.

3. Minimize the temporal penalty term by applying the NLM separately on the real and imaginary time curves of the current complex image estimate and update the estimate: $\mathbf{m}^n_{TNL} = \mathbf{m}^n_{data} + \alpha(NL_T(\mathbf{m}^n_{data}) - \mathbf{m}^n_{data})$, α is the relaxation parameter which is set between (0,2] to ensure convergence (44). NL_T represents the 1D temporal version of the filter in Eq. [1] applied on all time curves. The weights $\mathbf{w_t}$ are computed using $\mathbf{m}^n_{data}$ according to Eq. [2] but with 1D temporal neighborhoods.
4. Minimize the spatial penalty term by applying the NLM separately on the real and imaginary images of the current complex image estimate: $\mathbf{m}^n_{STNL} = \mathbf{m}^n_{TNL} + \alpha(NL_S(\mathbf{m}^n_{TNL}) - \mathbf{m}^n_{TNL})$. NL_S represents the 2D spatial version of the filter in Eq. [1] applied on all time frames. The weights $\mathbf{w_s}$ are computed using $\mathbf{m}^n_{TNL}$ according to Eq. [2] with 2D spatial neighborhoods.
5. Initialize the next iteration with the new image from all three constraints: $\mathbf{m}^{n+1} = \mathbf{m}^n_{STNL}$.

Steps (2–5) are repeated until the difference between new image estimate, $\mathbf{m^{n+1}}$ and current image $\mathbf{m^n}$ is below a certain threshold or a certain maximum number of iterations is reached.

For 3D dynamic tumor imaging, 3D *k*-space data are acquired at each time frame. In order to reduce the computation time, we perform a 1D Inverse Fourier Transform (IFT) along the fully sampled readout dimension of each 3D data frame and process the 2D slices of phase encoded data separately. Processing with 3D data was slower by ≈15% than calculating all of the slices separately and has higher memory burden than cropping in the read dimension and using 2D FTs. Since the computationally intensive neighborhood constraints are applied on image estimate **m**, using a joint multicoil approach saves reconstruction time and yields improved results. This is in contrast to reconstructing individual coil images separately and combining them.

The parameters for the reconstruction are as follows. For computing the weights $\mathbf{w_t}$ and $\mathbf{w_s}$, search window size = 7, comparison window size = 5, and square neighborhoods were chosen for the spatial case. The decay parameter for the weights, *h*, was chosen as $0.2\sigma_t$ for temporal, and $0.05\sigma_s$ for spatial penalty terms. σ_t and σ_s represent the temporal and spatial standard deviations of pixel intensities in the background region of the undersampled real images reconstructed with IFT. The initial estimate $\mathbf{m^0}$ was chosen by combining complex IFT images of the undersampled data from different coils (45). α was chosen as 0.1. These parameters were empirically chosen using one fully sampled dataset as the gold standard and sensitivity of results to the parameters is presented in the Discussion section.

In Vivo DCE Data

Fully sampled raw *k*-space data were acquired with a Siemens scanner using a 3D spoiled gradient echo sequence in four breast cancer patients and one brain tumor patient. For the bilateral breast data acquisition with left to right read direction, scan parameters were TR = 2.35–3.16 msec, TE = 0.99–1.24 msec, flip angle = 10–15°. A seven channel dedicated breast coil was used. The acquisition matrix, kx-ky-kz-t, varied between 256 × (80–104) × 80 × (42–60). Temporal resolution was 12–15 seconds and 6/8 partial Fourier was used in ky and kz. 0.1 mL/kg dose of Omniscan was injected at a rate of 4 mL/sec followed by a 20-mL saline flush at a rate of 2 mL/sec. For the brain acquisition TR = 2.82 msec, TE = 1.04 msec, flip angle = 17°. Acquisition matrix was 256 × 70 × 26 × 60 with 6/8 partial Fourier in ky and kz. The temporal resolution was 5 seconds. Informed consent was

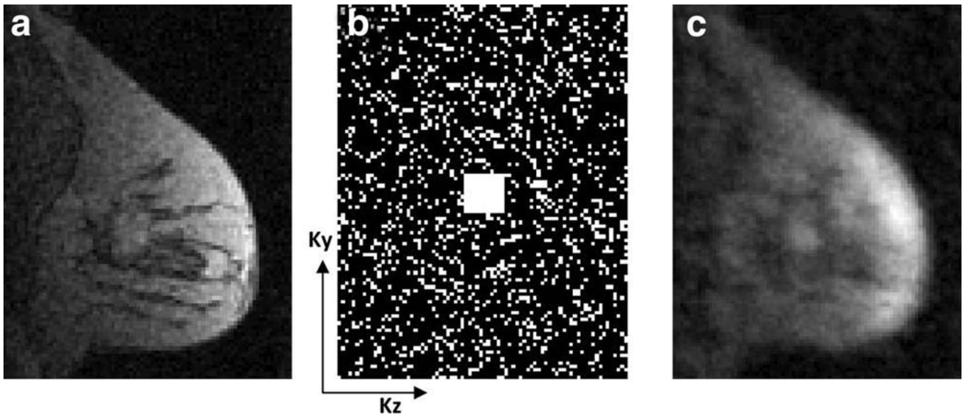

Figure 2. Illustration of undersampling. **(a)** Single time frame for a sagittal slice from a 3D DCE sequence for a breast dataset from a single coil. **(b)** Undersampling pattern in ky-kz space for a single time frame. The white region represents the phase encodes that are kept. **(c)** Corresponding IFT reconstruction of the undersampled data.

obtained and all patient data were acquired in accordance with the Institutional Review Board guidelines.

In order to test the NLM constrained reconstruction approach, data for each coil were undersampled offline in a variable density fashion in which nine contiguous central phase encoding lines in each of nine central planes in 3D *k*-space were kept and the phase encodes in the outer planes were discarded in a uniformly random pattern for each time frame. The ky-kz sampling pattern for a single time frame is shown in Fig. 2. This type of sampling pattern produces "softer" artifacts as compared to those arising from an interleaved undersampling pattern. Figure 2a,c shows the fully sampled and undersampled images, respectively, of a single slice of breast data from a single timepoint from a single coil reconstructed using IFT. The undersampled image is blurry and has noise-like artifacts as opposed to discrete ghosts found with interleaved undersampling. For both breast and brain datasets the last time frame in the dynamic sequences was generated by a sliding window reconstruction as outlined below in order to obtain the coil sensitivity information. Each individual complex coil image was divided by the sum-of-squares image and fit to a third-order polynomial to obtain the sensitivity information (11).

Comparison to Existing Methods

Total Variation Constrained Reconstruction

We compare the nonlocal means approach to the TV constrained reconstruction with spatial and temporal constraints. The 2D L_1 norm spatial constraint (total variation) is given by $\| \sqrt{\nabla_x \mathbf{m}^2 + \nabla_y \mathbf{m}^2} \|_1$, where ∇_x and ∇_y are spatial gradients in x and y, respectively. The corresponding temporal constraint is given by $\| \nabla_t \mathbf{m} \|_1$ where ∇_t is the gradient along time dimension for each pixel. Reconstruction is performed iteratively by minimizing the cost functional consisting of the multicoil data fidelity term in Eq. [5] but using the total variation constraints on the image estimate. A gradient descent approach was used for the minimization process (28). We note that when the data $\mathbf{D}$ are fully sampled according to the Nyquist limit, this is equivalent to the original TV application for denoising. POCS-based alternating minimization can also be applied to the TV constrained reconstruction. Typically a few iterations of gradient descent or conjugate gradient are performed for the TV minimization in a serial POCS framework (46).

Sliding Window Reconstruction

We also compare the NLM reconstruction to the noniterative sliding window reconstruction method. In this method, for a given time frame, the missing phase encoding lines in 3D *k*-space are filled in from the nearest sampled *k*-space lines in neighboring time frames to give a full 3D *k*-space at each time frame. After filling in the missing *k*-space data for multiple coils, 3D IFT was applied and the individual coil images were combined using the complex coil sensitivities (45).

Evaluation of Reconstructions

Reconstructed images from undersampled data were compared qualitatively as well as quantitatively to fully sampled ground truth images. Difference images were computed and visual analysis was done to identify residual artifacts and loss of any information. Mean signal intensity time curves in different enhancing regions were computed and compared. Quantitative analysis was done in terms of SNR indices and root mean square (RMS) errors. An SNR index was computed as μ/σ; μ is the mean signal estimate computed from the average of signal from a uniform region in two different time frames in the dynamic sequence and σ is the standard deviation of the difference in signals obtained from the same region of interest (47). The regions used are from gray matter or soft tissue regions and the calculated SNRs are most useful for comparison between the methods since noise varies spatially in these reconstructions (48).

RESULTS

Breast Imaging

Figure 3 shows the results of reconstructions of a sagittal slice using the NLM based approach and compares the NLM results with TV and sliding window reconstruction methods. Figure 3a–g compares the spatial characteristics and Fig. 3h–k compares the temporal characteristics. The NLM and sliding

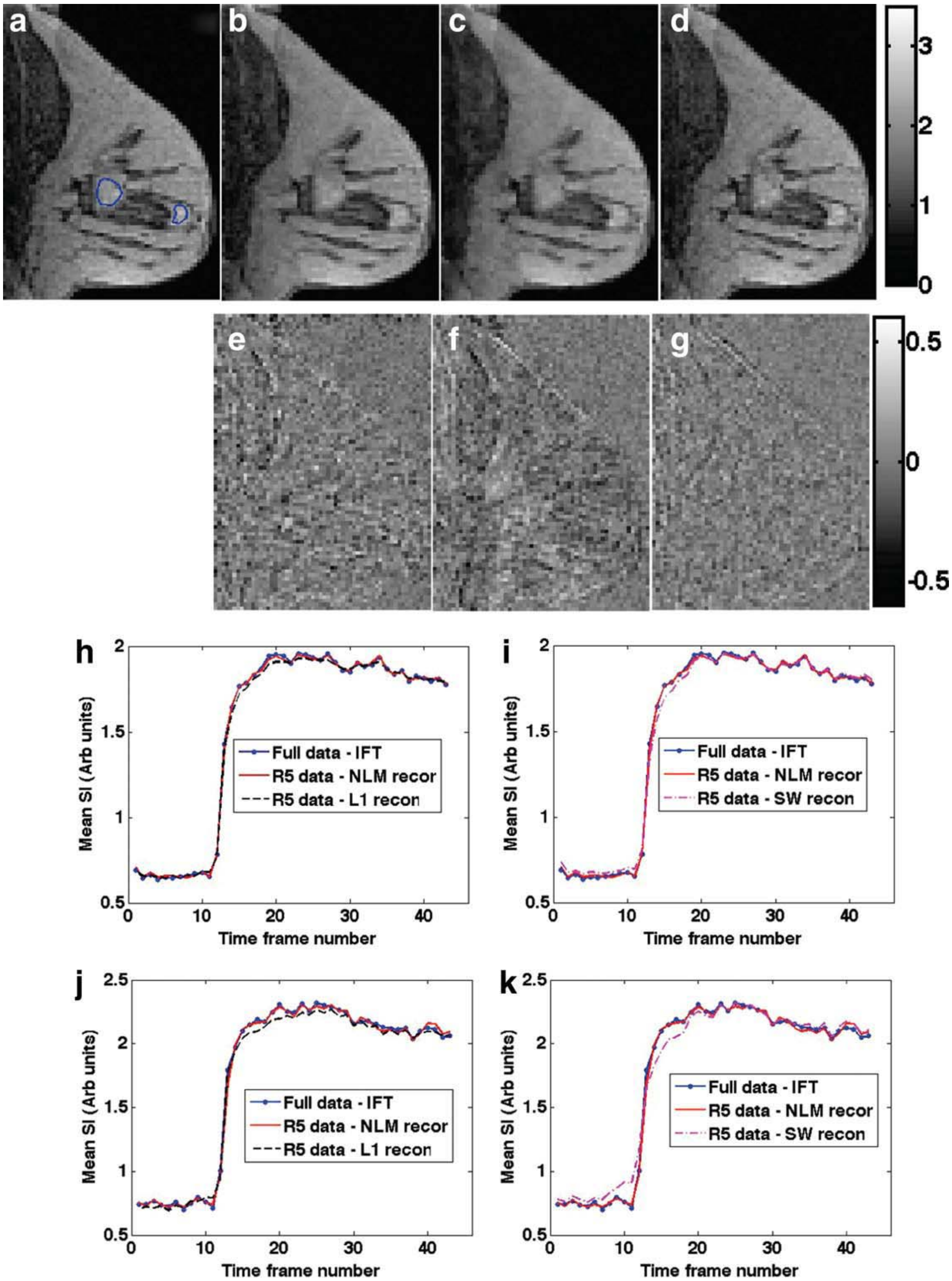

Figure 3. Comparison of breast data reconstructions: spatial and temporal characteristics. **(a)** Single time frame reconstructed using IFT from fully sampled data from all coils with complex coil sensitivities. ROIs are circled in the tumors. **(b)** NLM multicoil reconstruction image from R = 5 data. **(c)** TV multicoil reconstruction from R = 5 data. **(d)** Corresponding sliding window image from R = 5 data. **(e)** Difference image (a–b). **(f)** Difference image (a–c). **(g)** Difference image (a–d). **(h,i)** Comparison of mean intensity time curves for large tumor ROI for: (h) full data, NLM and TV reconstructions (i) full data, NLM and SW reconstructions. **(j,k)** Corresponding time curves for small tumor ROI curves. [Color figure can be viewed in the online issue, which is available at wileyonlinelibrary.com.]

window time frames are less pixelated and have overall improved contrast and higher fidelity to Fig. 3a than the TV reconstruction. The difference image corresponding to NLM reconstruction has fewer defined structures as compared to the TV method, suggesting more faithful preservation of spatial features. In terms of temporal characteristics, time curves from the NLM reconstructions for both of the tumors match the true time curves better than the time curves from the TV reconstructions. While the sliding

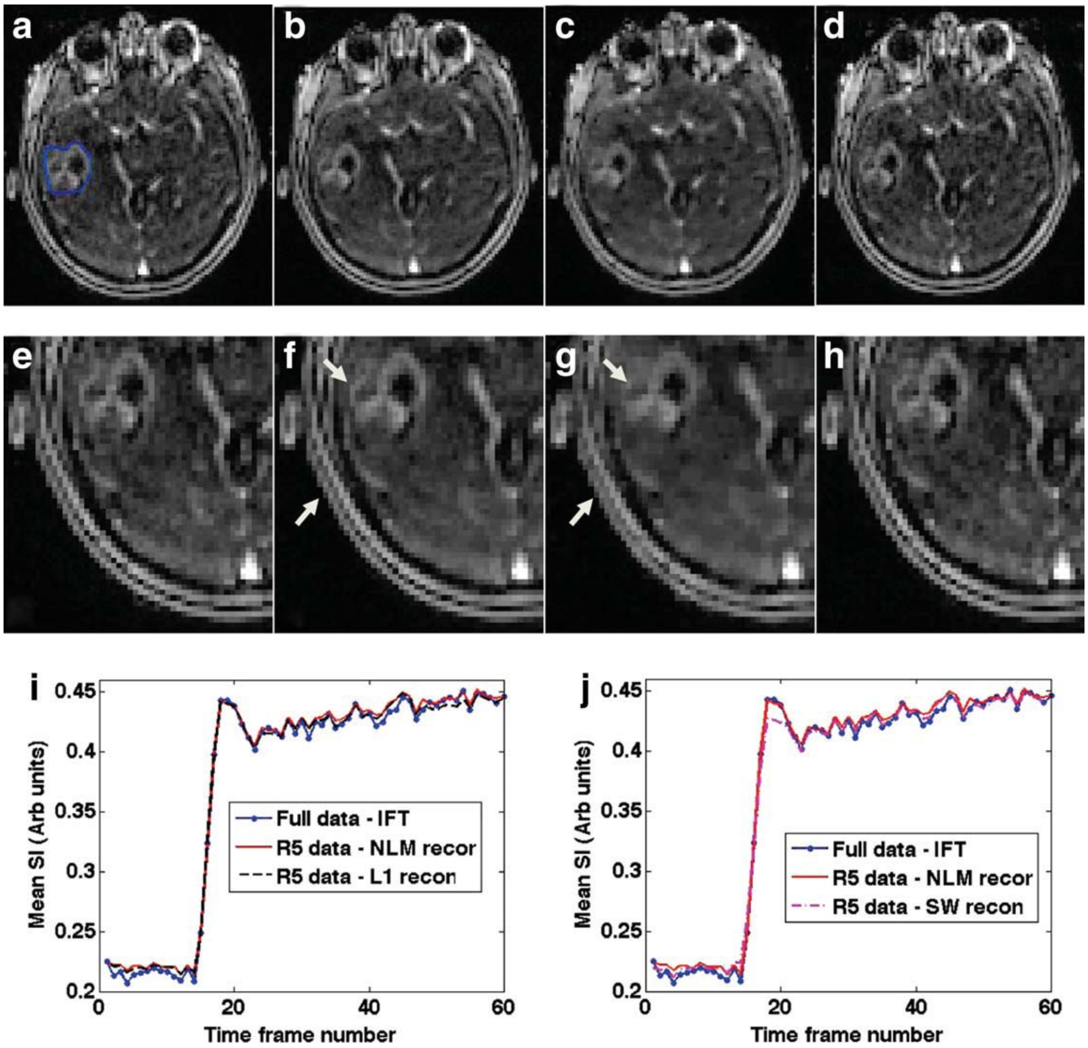

Figure 4. Comparison of brain data reconstructions: spatial and temporal characteristics. **(a)** Single time frame reconstructed using IFT from fully sampled data with a region of interest encircling the tumor (arrow). **(b)** NLM multicoil reconstruction image from R = 5 data. **(c)** TV multicoil reconstruction from R = 5 data. **(d)** Corresponding sliding window image from R = 5 data. **(e–h)** Zoomed images corresponding to (a–d) respectively. The corresponding arrows in (f,g) point to the differences in the images. **(i,j)** Comparison of mean intensity time curves from the ROI for: (i) full data, NLM and TV reconstructions (j) full data, NLM and SW reconstructions. [Color figure can be viewed in the online issue, which is available at wileyonlinelibrary.com.]

window result in Fig. 3d visually matches the true reconstruction spatially, its performance is poor in terms of preserving the crucial temporal characteristics. This is a known limitation of this view-sharing method, which causes temporal blurring of rapidly varying signals (15,16). This temporal blurring is more prominent in Fig. 3k, which compares the curves for the smaller tumor ROI. The baseline intensities for the sliding window curves are also elevated due to the fact that for the initial time frames the missing data are taken only from the future time frames. Even though the data are undersampled by a factor of five since variable density sampling pattern is used, some data are filled in from more than five frames apart. Mean SNR index over all the four datasets was computed by taking an ROI from the uniform soft tissue. For NLM and TV reconstructions it was higher than fully sampled images by 23.5% (±14.3) and 27% (±30), respectively. For SW reconstruction it was lower than full data reconstruction by 7.3% (±6.1). The mean RMS error for the NLM method was lower than TV by 8.9% (±3.6) and was lower than SW by 10.3% (±13.1).

Brain Imaging

Figure 4 compares the three undersampled reconstructions and the fully sampled image on an axial slice. Fidelity in terms of spatial characteristics is higher for the NLM image than the TV reconstructed image. This difference can be appreciated better in the zoomed images. The arrows point to fine structures in the images that are lost and have poor contrast in the TV image. This type of loss can affect not only the visual analysis but also pixelwise quantitative analysis (9,10). NLM and TV methods preserve the temporal characteristics of the fully sampled data and outperform the sliding window method as shown

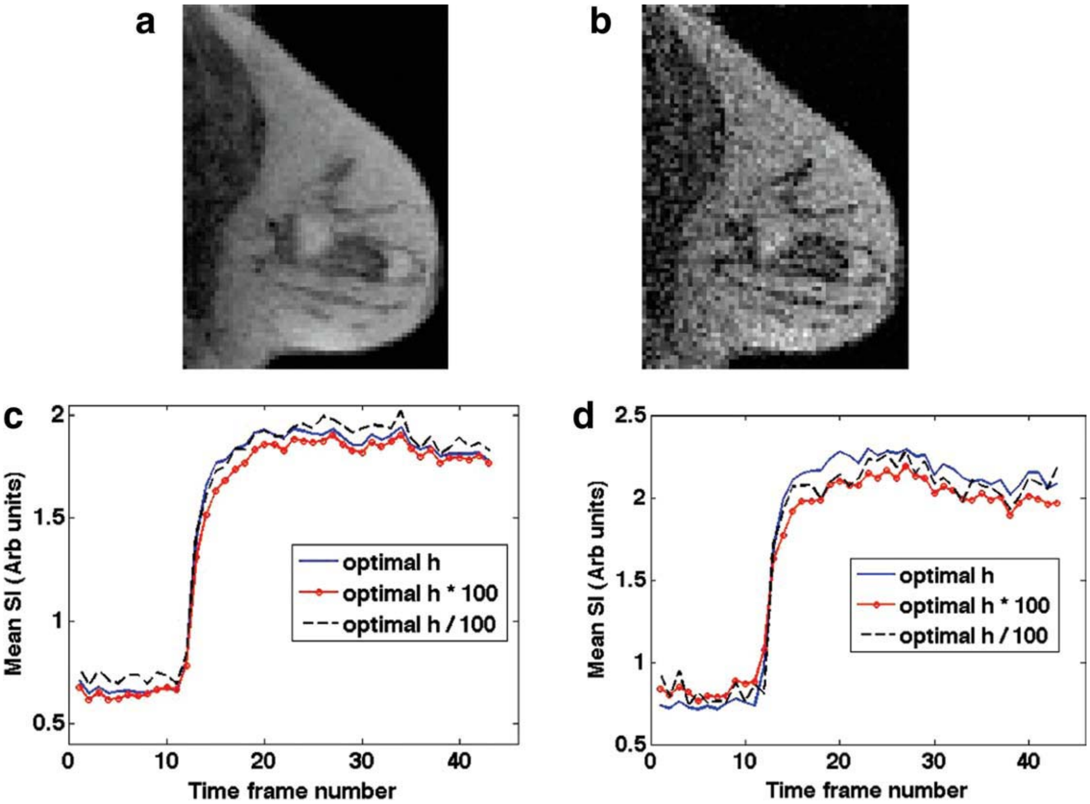

Figure 5. Effect of decay control parameter "*h*": **(a)** Image corresponding to 100 times the optimal "*h*" values for both temporal and spatial constraints. **(b)** Image corresponding to 1/100 times the optimal "*h*" values for both temporal and spatial constraints. **(c)** Comparison of mean intensity curves for the large tumor ROI in Fig. 3a. **(d)** Comparison of mean intensity time curves for the small tumor ROI in Fig. 3a. [Color figure can be viewed in the online issue, which is available at wileyonlinelibrary.com.]

in Fig. 4j. RMS errors for TV and SW images were comparable. NLM's RMS error was lower than TV and SW images by 12%. The SNR index in the gray matter region for both the NLM and TV reconstructions was higher than fully sampled reconstructions by 41% and 28%, respectively. For SW reconstruction, the SNR index was comparable to full data reconstruction (within 2%).

DISCUSSION

NLM-based reconstruction offers a promising way to obtain quality images from severely undersampled DCE tumor data. Unlike gradient-based constraints that ensure similarity of adjacent pixels, the current approach is based on a more realistic neighborhood similarity model for MR images.

Reconstruction Parameters

The NLM-constrained reconstruction, like most iterative reconstruction methods, has several parameters that need to be chosen carefully to obtain good results. The most important part in the reconstruction is the computation of weights $\mathbf{w}_t$ and $\mathbf{w}_s$ in steps 3 and 5. For computing these weights, optimal choice of the window sizes depends on image resolution and these windows form the key idea of the nonlocal approach. Choosing a very large search window may not be optimal, as it not only increases computation time but also can result in inclusion of unwanted neighborhoods, albeit with low weights. Choosing too large of a comparison window results in finding fewer neighborhoods that are similar and can result in incomplete suppression of the aliasing artifacts.

When individual pixels are compared for similarity solely in terms of their intensities as opposed to their similarity in neighborhoods around them (or equivalently, the neighborhoods become single points), the NLM approach reduces to an application of the bilateral filter (49). It was recently reported for nondynamic MR reconstruction that using a bilateral filter in an iterative fashion while preserving data fidelity is equivalent to homotopic minimization of the L_0 norm of the underlying signal (50). The results with the bilateral filter were reported to be comparable to the L_1 norm/TV approach (50). The framework presented here is based on a more general filter and results in improvements over the L_1 norm/TV approach for 3D dynamic MR images. For the tumor datasets here with spatial resolution in the phase-encode directions ranging from 1.5–2 × 1.5–2 mm^2 and temporal resolution ranging from 6–15 seconds, an empirically determined search window size of 7 and comparison window size of 5 for computing the weights gave good results. Although not shown here, the reconstructions were robust to variations (±2) in the window sizes.

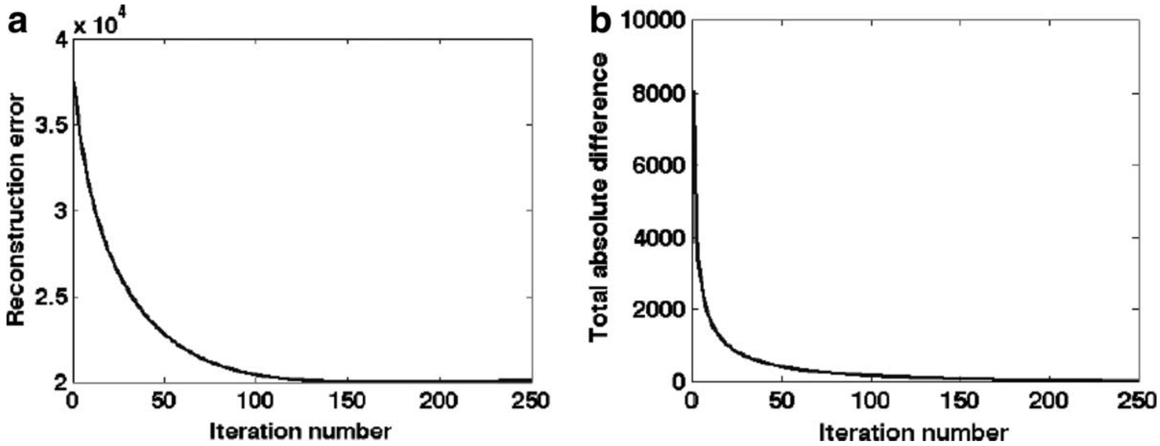

Figure 6. Illustration of convergence of the NLM reconstruction. **(a)** Plot showing the reconstruction error (total absolute difference in pixel intensities) with iterations compared to full data reconstruction for the breast data. **(b)** Plot showing the total absolute difference between the current and previous iteration image estimates for the breast data.

Another important parameter is the decay parameter, *h*, which controls the relative weighting of the distance between neighborhoods. Choosing a large value for *h* results in a slower decay rate of the neighborhood distance and results in excessive smoothing in the reconstruction. On the other hand, choosing a very small *h* results in inclusion of very few neighborhoods with significant weights, leading to incomplete artifact suppression. Figure 5 compares the spatial and temporal characteristics of the reconstructed images when *h* is varied for both $\mathbf{w_t}$ **and** $\mathbf{w_s}$. The images and the time curves are oversmoothed for a large *h*, while the results are noisy when a small value of *h* is chosen.

For all of the reconstructions here, convergence was achieved within 300 iterations, as shown in Fig. 6. The reconstruction error, as compared to full data reconstruction, drops substantially in the first few iterations and then at a slower rate in the later iterations. The same trend is also observed with the plot in Fig. 6b for the difference between the current image estimate, $\mathbf{m}^\mathbf{n}$ and the previous image estimate, $\mathbf{m}^{\mathbf{n}-1}$.

All of the reconstruction parameters were empirically determined using one dataset and were fixed for all other datasets and resulted in similar performance with graceful degradation in quality for nonoptimal parameters.

Spatial vs. Temporal Penalty Terms

In order to exploit the dynamic nature of the tumor imaging we model the spatial as well as the temporal characteristics of fully sampled images using neighborhood penalty terms and perform a joint multi-image reconstruction. This is in contrast to directly using parallel imaging techniques for accelerations where each time frame is reconstructed independently (11,12). Figure 7 compares the effects of temporal and spatial constraints separately towards artifact removal. While using each constraint independently results in partial recovery of the true image estimate, the joint approach results in overall superior quality. Also, the order in which the temporal and spatial

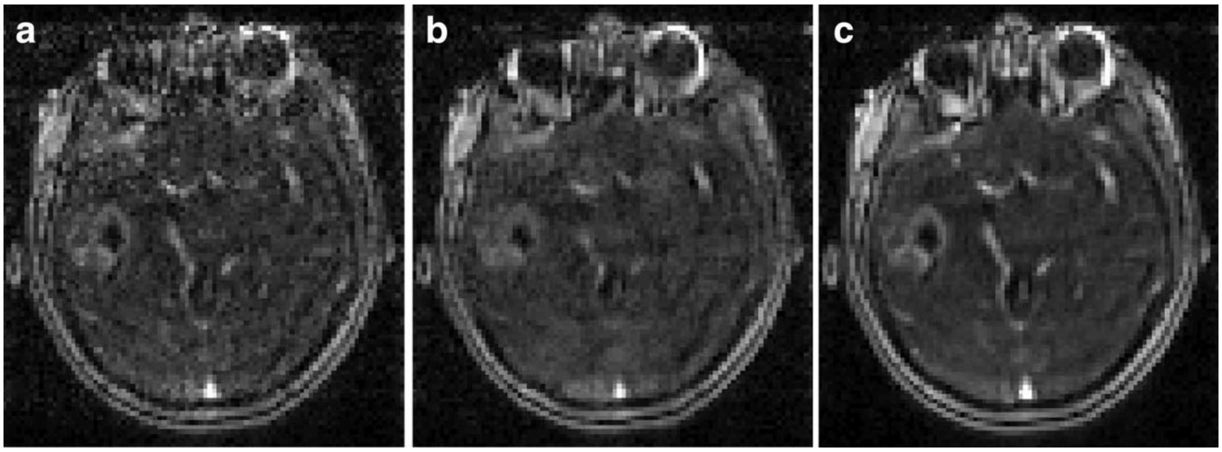

Figure 7. Spatial vs. temporal NLM constraints. **(a)** Image reconstructed using neighborhood penalty term only on the time curves. **(b)** Image reconstructed using only spatial neighborhood penalty on individual time frames. **(c)** Image with both spatial and temporal constraints is also shown for reference.

constraints are applied in the POCS framework did not make a significant difference in the final results.

There are alternative approaches towards modeling dynamic images, for example, using an NLM approach with an enhanced spatial window (51). In (51), a 3D search window was used, where the third dimension is time. This resulted in improved denoising performance even when motion is present between the time frames. Since there is minimal motion in the DCE tumor images and the enhanced spatial window method requires considerably more computation, we applied spatial and temporal windows separately. For dynamic MRI applications where motion is an issue, the enhanced spatial window may offer improved reconstructions.

Also, in Eqs. [3] and [4], while the weights $\mathbf{w_t}$ and $\mathbf{w_s}$ are computed using patch distances, we are minimizing the L_2 norm difference between a single pixel and individual pixels within a search window. An even more general neighborhood based penalty term can be used where the L_2 distance between patches within the search window is minimized (43).

Computation Time

Computation of weights $\mathbf{w_s}$ and $\mathbf{w_t}$ is the most computationally intensive part in the reconstruction. However, a number of approaches can be used together to make the approach feasible. First, the NLM reconstruction allows for parallel implementation on multicore processors. Steps 3 and 4 in the implementation were parallelized to run on an 8 processor machine with MatLab's (MathWorks, Natick, MA) parallel computing toolbox. We found an approximately linear increase in speed-up with number of processors. Also, the joint multicoil approach proposed is significantly faster than reconstructing each coil image separately (almost by a factor of number of coils), since the constraints are applied on the single image estimate $\mathbf{m}$, rather than an image estimate for each coil.

Here we break the 3D+time reconstruction task into a series of smaller 2D+time problems (with cropping in the read dimension) with two separate constraints to gain flexibility and reduce computational load. A more computationally intensive 3D NLM constraint can also be applied, in which similarity is enforced in terms of 3D cubes (y-z-t) around each pixel.

The proposed NLM reconstruction is also robust to the choice of initial estimate, $\mathbf{m^0}$. While IFT images from undersampled data are used for the initial estimate, the convergence to the final image can be accelerated by starting with an image closer to the final solution. We found improvements in the reconstruction time by a factor of three when the sliding window images are used for the initial estimate. It took ≈10 minutes to reconstruct a 80 × 64 × 44 dataset from a 7-coil undersampled DCE breast acquisition, on a 2.8 GHz 8-processor machine in MatLab starting with a sliding window initial estimate. While not implemented here, it has been reported that accelerations up to a factor of 45 can be achieved using multithreaded graphical processing units (GPUs) as compared to standard CPUs for NLM denoising (52). Similar speed-ups could be achieved for NLM reconstructions. Additional software approaches, for example, methods proposed previously (53,54), can be used in order to speed up computation of the weights for the reconstruction by selectively choosing the neighborhoods within the search window.

In conclusion, the NLM-constrained reconstruction approach offers a promising framework for improving 3D dynamic tumor imaging. The nonlocal constraints are based on a generalized model for MR images and can offer high-quality reconstruction from significantly undersampled data. Unlike the linear sliding window method and the nonlinear TV reconstruction approaches, the proposed method offers a better trade-off between temporal and spatial fidelity at high accelerations. While the reconstruction is computationally demanding, multipronged software and hardware technologies can be used to make it viable. The proposed method has the potential to improve the clinical utility of 3D DCE imaging of tumors.

REFERENCES

1. Padhani AR. Dynamic contrast-enhanced MRI in clinical oncology: current status and future directions. J Magn Reson Imaging 2002;16:407–422.
2. Barrett T, Brechbiel M, Bernardo M, Choyke PL. MRI of tumor angiogenesis. J Magn Reson Imaging 2007;26:235–249.
3. Hayes C, Padhani AR, Leach MO. Assessing changes in tumor vascular function using dynamic contrast-enhanced magnetic resonance imaging. NMR Biomed 2002;15:154–163.
4. Daldrup-Link HE, Rydland J, Helbich TH, et al. Quantification of breast tumor microvascular permeability with feruglose-enhanced MR imaging: initial phase II multicenter trial. Radiology 2003;229:885–892.
5. Delille J-P, Slanetz PJ, Yeh ED, Halpern EF, Kopans D, Garrido L. Invasive ductal breast carcinoma response to neoadjuvant chemotherapy: noninvasive monitoring with functional MR imaging-pilot study. Radiology 2003;228:63–69.
6. Schnall MD, Ikeda DM. Lesion Diagnosis Working Group report. J Magn Reson Imaging 1999;10:982–990.
7. Roberts HC, Roberts TP, Bollen AW, et al. Correlation of microvascular permeability derived from dynamic contrast-enhanced MR imaging with histologic grade and tumor labeling index: a study in human brain tumors. Acad Radiol 2001;8:384–391.
8. Turnbull LW. Dynamic contrast-enhanced MRI in the diagnosis and management of breast cancer. NMR Biomed 2009;22:28–39.
9. Larsson HB, Stubgaard M, Frederiksen JL, Jensen M, Henriksen O, Paulson OB. Quantitation of blood-brain barrier defect by magnetic resonance imaging and gadolinium-DTPA in patients with multiple sclerosis and brain tumors. J Magn Reson Imaging 1990;16:117–131.
10. Tofts PS, Kermode AG. Measurement of the blood-brain barrier permeability and leakage space using dynamic MR imaging. 1. Fundamental concepts. Magn Reson Med 1991;17:357–367.
11. Pruessmann KP, Weiger M, Scheidegger MB, Boesiger P. SENSE: sensitivity encoding for fast MRI. Magn Reson Med 1999;42: 952–962.
12. Griswold MA, Jakob PM, Heidemann RM, et al. Generalized autocalibrating partially parallel acquisitions (GRAPPA). Magn Reson Med 2002;47:1202–1210.
13. Friedman PD, Swaminathan SV, Smith R. SENSE imaging of the breast. AJR Am J Roentgenol 2005;184:448–451.
14. van Vaals JJ, Brummer ME, Dixon WT, et al. "Keyhole" method for accelerating imaging of contrast agent uptake. J Magn Reson Imaging 1993;3:671–675.
15. Song HK, Dougherty L. Dynamic MRI with projection reconstruction and KWIC processing for simultaneous high spatial and temporal resolution. Magn Reson Med 2004;52:815–824.

16. Hu. X. On the “keyhole” technique. J Magn Reson Imaging 1994; 4:231.
17. Madore B, Glover GH, Pelc NJ. Unaliasing by fourier-encoding the overlaps using the temporal dimension (UNFOLD), applied to cardiac imaging and fMRI. Magn Reson Med 1999;42: 813–828.
18. DiBella EVR, Wu YJ, Alexander AL, Parker DL, Green D, McGann CJ. Comparison of temporal filtering methods for dynamic contrast MRI myocardial perfusion studies. Magn Reson Med 2003; 49:895–902.
19. Tsao J, Boesiger P, Pruessmann KP. k-t BLAST and k-t SENSE: dynamic MRI with high frame rate exploiting spatiotemporal correlations. Magn Reson Med 2003;50:1031–1042.
20. Dougherty L, Isaac G, Rosen MA, et al. High frame-rate simultaneous bilateral breast DCE-MRI. Magn Reson Med 2007;57: 220–225.
21. Kellman P, Epstein FH, McVeigh ER. Adaptive sensitivity encoding incorporating temporal filtering (TSENSE). Magn Reson Med 2001;45:846–852.
22. Han M, Daniel BL, Hargreaves BA. Accelerated bilateral dynamic contrast-enhanced 3D spiral breast MRI using TSENSE. J Magn Reson Imaging 2008;28:1425–1434.
23. Martel AL, Chan RW, Ramsay E, Plewes DB. Removing undersampling artifacts in DCE-MRI studies using independent components analysis. Magn Reson Med 2008;59:874–884.
24. Mistretta CA, Wieben O, Velikina J, et al. Highly constrained backprojection for time-resolved MRI. Magn Reson Med 2006;55: 30–40.
25. Fain SB, Wieben O, Wu Y, Mistretta CA, Brittain J, Kelcz F. Highly constrained backprojection: a method for high spatial and temporal resolution in DCE-MRI of breast cancer. In: Proc 14th Annual Meeting ISMRM, Seattle; 2006. p 3474.
26. Block KT, Uecker M, Frahm J. Undersampled radial MRI with multiple coils. Iterative image reconstruction using a total variation constraint. Magn Reson Med 2007;57:1086–1098.
27. Lustig M, Donoho DL, Pauly JM. Sparse MRI: the application of compressed sensing for rapid MR imaging. Magn Reson Med 2007;58:1182–1195.
28. Adluru G, McGann C, Speier P, Kholmovski EG, Shaaban A, DiBella EVR. Acquisition and reconstruction of undersampled radial data for myocardial perfusion MRI. J Magn Reson Imaging 2009;29:466–473.
29. Rudin LI, Osher S, Fatemi E. Nonlinear total variation based noise removal algorithms. Physica D 1992;60:259–268.
30. McGraw T, Vemuri BC, Chen Y, Rao M, Mareci T. DT-MRI denoising and neuronal fiber tracking. Med Image Anal 2004;8: 95–111.
31. Candes E, Romberg J, Tao T. Robust uncertainty principles: exact signal reconstruction from highly incomplete frequency information. IEEE Trans Info Theory 2006;52:489–509.
32. Donoho DL. Compressed sensing. IEEE Trans Info Theory 2006; 52:1289–1306.
33. Chan T, Marquina A, Mulet P. High-order total variation based image restoration. SIAM J Sci Compute 2000;22:503–516.
34. Strong D, Chan T. Edge-preserving and scale-dependent properties of total variation regularization. Inverse Problems 2003;19: S165–S187.
35. Buades A, Coll B, Morel JM. A review of image denoising algorithms, with a new one. Multiscale Model Simul 2005;4:490–530.
36. Awate S, Whitaker RT. Unsupervised, information-theoretic, adaptive image filtering with applications to image restoration. IEEE Trans Pattern Anal Mach Intell 2006;28:364–376.
37. Manjón JV, Carbonell-Caballero J, Lull JJ, García-Martí G, Martí-Bonmatí L, Robles M. MRI denoising using non-local means. Med Image Anal 2008;12:514–523.
38. Coupé P, Yger P, Prima S, Hellier P, Kervrann C, Barillot C. An optimized blockwise non local means denoising filter for 3D magnetic resonance images. IEEE Trans Med Imaging 2008;27:425–441.
39. Manjón JV, Thacker NA, Lull JJ, Garcia-Martí G, Marti-Bonmati L, Robles M. Multicomponent MR image denoising. Int J Biomed Imaging 2009;2009:756897.
40. Naegel B, Cernicanu A, Hyacinthe JN, Tognolini M, Vallée JP. SNR enhancement of highly-accelerated real-time cardiac MRI acquisitions based on non-local means algorithm. Med Image Anal 2009;13:598–608.
41. Adluru G, Tasdizen T, Whitaker RT, DiBella EVR. Improved undersampled MRI reconstruction using non-local means. Int Conf Pattern Recognition, IAPR, August 23–26. 2010; Istanbul, Turkey (in press).
42. Marks RJ II. Alternating projections onto convex sets. In: Jansson PA, editor. Deconvolution of images and spectra, 2nd ed. Orlando, FL: Academic Press; 1996. p 476–501.
43. Protter M, Elad M, Takeda H, Milanfar P. Generalizing the non local-means to super-resolution reconstruction. IEEE Trans Image Proc 2009;18:36–51.
44. Gubin LG, Polyak BT, Raik EV. The method of projections for finding the common point in convex sets. USSR Comput Math Phys 1967;7:1–24.
45. Roemer PB, Edelstein WA, Hayes CE, Souza SP, Mueller OM. The NMR phased array. Magn Reson Med 1990;16:192–225.
46. Sidky EY, Pan X. Image reconstruction in circular cone-beam computed tomography by constrained, total-variation minimization. Phys Med Biol 2008;53:4777–4807.
47. Reeder SB. Measurement of signal-to-noise ratio and parallel imaging. In: Schoenberg SO, Dietrich O, Reiser MF, editors. Parallel imaging in clinical MR applications. Berlin, Heidelberg: Springer; 2007. p 49–61.
48. Kellman P, McVeigh ER. Image reconstruction in SNR units: a general method for SNR measurement. Magn Reson Med 2005; 54:1439–1447.
49. Tomasi C, Manduchi R. Bilateral filtering for gray and color images. Sixth International Conference on Computer Vision; Bombay, India; 1998. p 839–846.
50. Trzasko J, Manduca A, Borisch E. Robust kernel methods for sparse MR image reconstruction. Med Image Comput Comput Assist Interv 2007;10(Pt 1):809–816.
51. Buades A, Coll B, Morel JM. Nonlocal image and movie denoising. Int J Comp Vision 2008;76:123–139.
52. Huang K, Zhang D, Wang K. Non-local means denoising algorithm accelerated by GPU. Medical Imaging, Parallel Processing of Images, and Optimization Techniques, SPIE, October 2009; Yichang, China. p 749711.
53. Mahmoudi M, Sapiro G. Fast image and video denoising via nonlocal means of similar neighborhoods. IEEE Signal Proc Lett 2005;12:839–842.
54. Tasdizen. T. Principal neighborhood dictionaries for non-local means image denoising. IEEE Trans Image Proc 2009;18: 2649–2660.